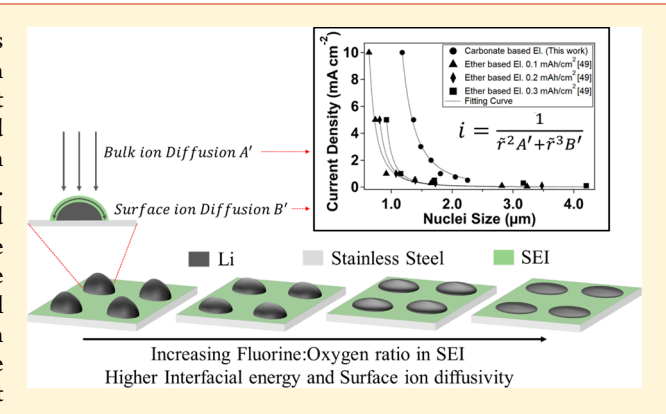


# Nucleation and Early Stage Growth of Li Electrodeposits

Prayag Biswal,<sup>†</sup> Sanjuna Stalin,<sup>†</sup> Atsu Kludze,<sup>†</sup> Snehashis Choudhury,<sup>§</sup> and Lynden A. Archer\*,<sup>†</sup>,<sup>‡</sup>

Supporting Information

**ABSTRACT:** The morphologies that metal electrodeposits form during the earliest stages of electrodeposition are known to play a critical role in the recharge of electrochemical cells that use metals as anodes. Here we report results from a combined theoretical and experimental study of the early stage nucleation and growth of electrodeposited lithium at liquid-solid interfaces. The spatial characteristics of lithium electrodeposits are studied via scanning electron microscopy (SEM) in tandem with image analysis. Comparisons of Li nucleation and growth in multiple electrolytes provide a comprehensive picture of the initial nucleation and growth dynamics. We report that ion diffusion in the bulk electrolyte and through the solid electrolyte interphase (SEI) formed spontaneously on the metal play equally important roles in regulating Li nucleation and growth. We show further



that the underlying physics dictating bulk and surface diffusion are similar across a range of electrolyte chemistries and measurement conditions, and that fluorinated electrolytes produce a distinct flattening of Li electrodeposits at low rates. These observations are rationalized using X-ray photoelectron spectroscopy (XPS), electrochemical impedance spectroscopy (EIS), and contact angle goniometry to probe the interfacial chemistry and dynamics. Our results show that high interfacial energy and high surface ion diffusivity are necessary for uniform Li plating.

KEYWORDS: Lithium metal anode, nucleation and growth, surface ion diffusion, interfacial energy

ithium (Li) metal is among the most promising anode batteries due to its extremely high theoretical specific capacity (3860 mAh g<sup>-1</sup>), most negative electrochemical potential (-3.040 V versus standard hydrogen electrode), and low density (0.534 g cm<sup>-3</sup>).<sup>1</sup> Rechargeable Li metal batteries (LMBs) have been extensively studied for over 40 years for prospective applications in portable electronics, electric vehicles, and grid-scale energy storage, though not yet commercialized. 1-4 These studies have revealed multiple shortcomings of Li metal anodes, including the metal's tendency to deposit during charging in low-density mossy morphologies, loosely termed dendrites; its low reversibility and poor Columbic efficiency (CE) in liquid electrolyte media; propensity to proliferate in the interelectrode space to shortcircuit the battery producing thermal runaway 1-6 and to undergo large volume changes during repeated cycles of charge and discharge. The "dendritic/mossy" growth of Li exacerbates all of these problems and, additionally, imparts fragility to the metal electrodeposits that can cause them to break away from the electronic circuitry of an electrode, producing so-called "orphaned/dead" Li. The orphaned Li has recently been reported to play an important, perhaps even dominant, role in the poor reversibility and low CE of Li metal anodes.

Significant experimental 1,3,5-9,13 and theoretical 10-13 efforts have been made in recent years to understand and control mossy/dendritic Li electrodeposition. The electrodeposition is presently understood to be destabilized at current densities, i, below the classical diffusion limiting value  $(i_L = 4FcD_+/\delta_D)$  by at least two processes: (i) morphological instability produced by heterogeneous nucleation of Li deposits in less passivated (faster ion transport) regions of an electrode; 5,7 and (ii) metal extrusion due to heterogeneous interfacial stresses, which produces root-growth of fibrous structures.  $^{8,12,14}$  For  $i > i_L$ morphological instability couples to the classical hydrodynamic instability known as electroconvection to produce much faster dendrite growth. 15 A variety of technical approaches have correspondingly been reported to be effective in eliminating/ slowing Li dendrite proliferation by addressing one or more of these instability modes. Among the most effective are: (i) liquid electrolytes containing additives that change the chemistry and transport properties of the solid-electrolyte interphase (SEI) formed in contact with Li; 16-22 (ii) artificial SEIs which simultaneously passivate the Li surface and enable

Received: August 28, 2019 Revised: September 19, 2019 Published: September 30, 2019

Α

<sup>&</sup>lt;sup>†</sup>Robert Frederick Smith School of Chemical and Biomolecular Engineering and <sup>‡</sup>Department of Materials Science and Engineering, Cornell University, Ithaca, New York 14853, United States

<sup>§</sup>Department of Chemical Engineering, Stanford University, Stanford, California 94305, United States

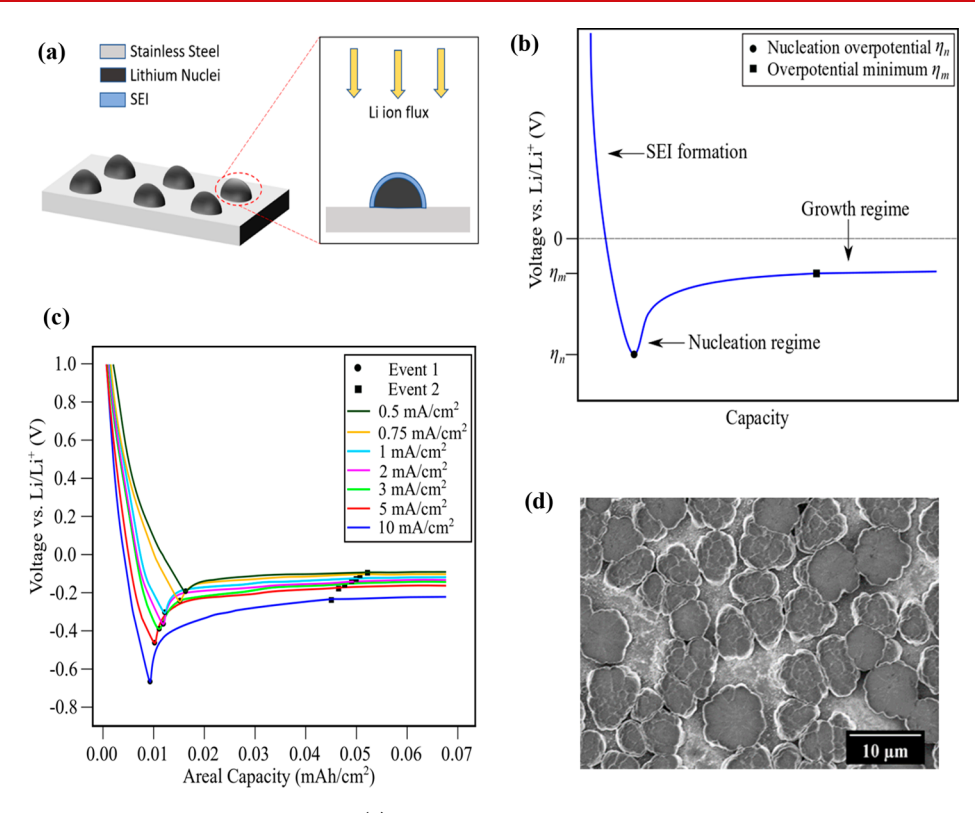


Figure 1. Fundamentals of lithium nucleation and growth. (a) Schematic showing electrodeposition of Li ion from the bulk electrolyte through the SEI on the stainless-steel substrate. (b) Schematic plot showing a typical voltage profile of galvanostatic Li deposition (black). Nucleation overpotential and overpotential minimum are marked by Event 1 and Event 2. (c) Experimental voltage profiles of galvanostatic Li deposition for a range of current densities. The electrolyte is 1 M LiPF<sub>6</sub> in EC/DMC (1:1 vol %). Nucleation overpotential and overpotential minimum are marked by Event 1 and Event 2. (d) SEM image of the electrodeposited lithium morphology captured at a current density of 0.5 mA/cm<sup>2</sup> and an areal capacity corresponding to that of overpotential minimum. The electrolyte is 1 M LiPF<sub>6</sub> in EC/DMC (1:1 vol %).

fast and less heterogeneous ion transport; 5,23-31 ion-transport regulators that may alter either the ion-flux to the electrode, size distribution the electrodeposit structures, or both;<sup>32-</sup> (iii) high-shear modulus solid and viscoelastic liquid electrolytes, which slow localized growth of dendritic structures by interfacial mechanical and/or polymer stresses; 38-43 and (iv) advanced current collectors that enable dissipation of localized stresses developed in the metal during deposition 14,44-46 or which facilitate continuous electrical connection and, thereby, electrochemical access to orphaned metal deposits. 44 Although the majority of these studies emphasize the ability to produce anodes with nondendritic morphology after several charge/ discharge cycles, the recent work by Zheng et al. 47 raises doubt about whether one is every truly able to achieve dendrite-free electrodeposition of Li on continuum length scales and in liquid electrolytes.

Here, we investigate the initial nucleation and growth dynamics of metallic lithium in liquid electrolytes with/without components believed to make the deposition nondendritic. We show that ionic diffusion in the solid—electrolyte interphase formed spontaneously on Li plays a crucial role in the development and growth of electrodeposited Li nuclei. We show further that by combining theoretical analysis of the early stage electrodeposit growth dynamics with experiments, it is possible to develop a comprehensive picture of the lithium electrodeposition process. The study builds upon the existing nucleation and growth framework proposed by Barton et al. and the recent work of Pei et al. to elucidate the role interphases formed on Li play in regulating ionic transport to the growing nuclei. Lithium ions are galvanostatically electro-

deposited onto a heterogeneous surface composed of polished stainless-steel (rms roughness =  $9.12 \pm 8.78$  nm) from the bulk electrolyte (Figure 1a). The electrodeposition is carried out at different current densities in carbonate liquid electrolytes with/without fluorinated carbonated additives reported to suppress the chemical and morphological instability of Li.  $^{18,50-52}$  The spatial characteristics (morphology, size, number density) of Li nuclei formed in the process are analyzed ex situ using scanning electron microscopy (SEM) and the interphases formed on the deposits studied using electrochemical impedance spectroscopy (EIS), goniometry, and X-ray photoelectron spectroscopy (XPS).

To form nuclei of a particular size r at an electrode, reduced metal ions at the electrode must overcome a nucleation barrier that can be conveniently manipulated by adjusting the electrochemical supersaturation at the electrified interface. A measurable physical parameter characteristic of the electrochemical supersaturation is the overpotential. 48,49,53,54 The driving force for nucleation may therefore be divided into three components: the charge transfer overpotential, diffusion overpotential, and interfacial (surface) energy overpotential. 48,49,53,54 An additional consideration in the nucleation of reactive metals like Li concerns barriers to ionic transport through the SEI formed spontaneously at the metal/electrolyte interface (Figure 1a). These effects are captured theoretically by extending the nucleation and growth model for noninteracting hemispherical nuclei proposed by Barton et al. 48 to account for SEI diffusion

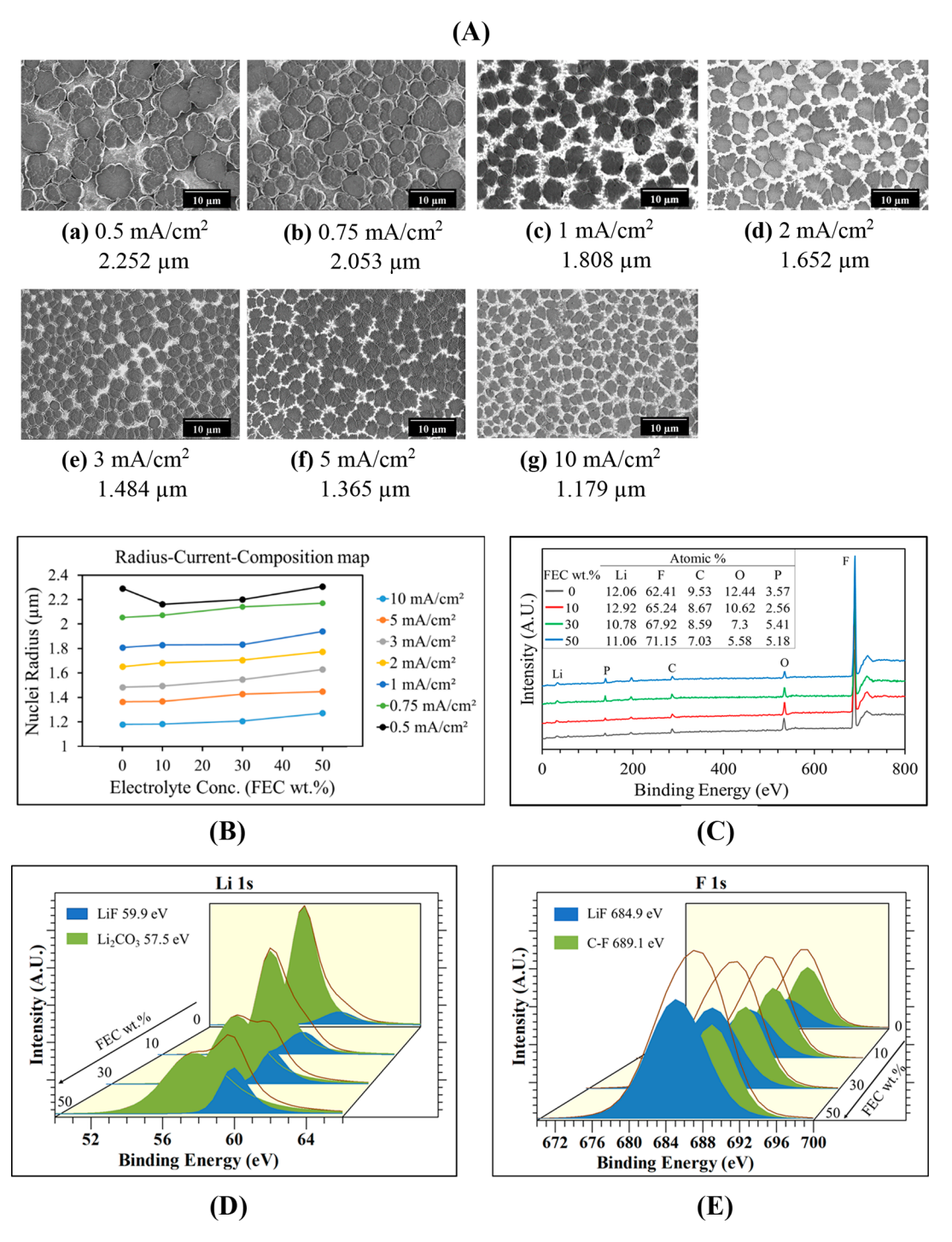


Figure 2. Effect of current density and electrolyte chemistry on the morphology and interfacial chemistry of lithium electrodeposits. (A) Ex situ SEM images of Li deposited on stainless-steel at current densities of (a) 0.5, (b) 0.75, (c) 1, (d) 2, (e) 3, (f) 5, and (g) 10 mA/cm², respectively. At lower current densities, the stainless-steel substrate is visible underneath the sparsely distributed Li nuclei. The electrolyte is 1 M LiPF<sub>6</sub> in EC/DMC (1:1 vol %). (B) Plot of nuclei radius for a range of current densities for varying concentration of FEC (0, 10, 30, 50 wt %) in 1 M LiPF<sub>6</sub> EC/DMC (1:1 vol %). (C) Chemical spectra of the SEI layer induced by varying concentrations of FEC (0, 10, 30, 50 wt %) in 1 M LiPF<sub>6</sub> EC/DMC (1:1 vol %). (D,E) Li 1s and F 1 spectra of the SEI layer induced by varying concentrations of FEC (0, 10, 30, 50 wt %) in 1 M LiPF<sub>6</sub> EC/DMC (1:1 vol %). The total areal capacity corresponds to that of overpotential minimum (Event 2).

$$\eta = \frac{RT}{\alpha F} \ln \frac{i}{i_0} + \frac{irRT}{D_B C_B F^2} + \frac{2\gamma V}{Fr} + \frac{ir^2 RT}{D_S C_S F^2}$$
 (1)

Here  $\eta$  is the net overpotential due to all of the processes referenced above; i and  $i_0$  are the current density and exchange current density respectively; r is the radius of the nuclei;  $D_{\rm B}$  and  $C_{\rm B}$  are the bulk electrolyte Li ion diffusivity and

concentration respectively;  $D_S$  and  $C_S$  are the SEI Li ion diffusivity and concentration respectively,  $\gamma$  is the interfacial energy, and  $\alpha$ , V, R, T, F are charge transfer coefficient, molar volume of metal, universal gas constant, temperature, and Faraday constant, respectively.

Deconvoluting each of these overpotential contributions from the voltage response during galvanostatic Li electro-

deposition is difficult as all are due to electrochemical processes occurring simultaneously. At current densities i <  $i_{\rm I}$ , the galvanostatic voltage response curve (Figure 1b) may nevertheless be divided into three distinct regimes: (1) An initial steep voltage drop, which is thought to be the result of reduction of the electrolyte components at the onset of electrode of polarization to produce an ion-conductive, solidstate electrolyte interphase (SEI) at the electrified interface. Because the SEI in typical carbonate liquids is self-limiting, for a clean heterogeneous interface with minimal intercalation or alloying the capacity corresponding to the SEI formation step is quite low. (2) A sharp voltage spike corresponding to formation of Li nuclei's at the electrified interface. The voltage spike reflects the electrochemical supersaturation needed to overcome the nucleation barrier. The voltage at the spike is therefore referred to as nucleation overpotential  $(\eta_n)$  and is marked as Event 1 in Figure 1b. The nucleation overpotential is a consequence of simultaneous charge transfer process and Li-solution interface formation process. Hence, it can be interpreted as a combination of charge transfer overpotential and interfacial formation overpotential. (3) A final regime in which the voltage initially rises before approaching a final plateau. This regime corresponds to the postnucleation growth phase. The overpotential is mainly due to mass-transfer of lithium ions from the bulk electrolyte through the SEI to the newly formed Li nuclei. The onset of voltage plateau is associated with an overpotential minimum  $(\eta_m)$ , marked as Event 2 in Figure 1b. The minimum has been reported to show a gradual transition of rate-limiting step from charge transfer/ interface formation controlled to mass transfer controlled.<sup>49</sup> The plateau following the overpotential minimum event can be attributed to a combination of bulk diffusion overpotential and SEI surface diffusion overpotential. Understanding how each of these three events is influenced by electrolyte chemistry is the focus of this study. Anticipating comparisons with SEM experiments of electrodeposits, we first consider the prediction of eq 1 for  $\eta_{\rm m}$ . Minimizing the net overpotential  $(\eta)$  with respect to the characteristic size (radius) of the nuclei, an inverse relationship between current density (i) and radius (r)of the nuclei is apparent (eq 2)

$$i = \frac{1}{\tilde{r}^2 A' + \tilde{r}^3 B'} \text{ where } A' = \frac{RT}{2\gamma V D_B C_B F} \text{ and } B' = \frac{RT}{\gamma V D_S C_S F}$$
 (2)

This minimum in the net overpotential is associated with a certain characteristic nuclei size,  $\tilde{r}$ , and a particular Li electrodeposition capacity (Figure 1b,c). Equation 2 indicates that ionic diffusion in the bulk is associated with the term quadratic in  $\tilde{r}$ , while ionic transport in the SEI is produces a stronger,  $\tilde{r}^3$  term in the current. Equation 2 also implies that the coefficients, A' and B', associated with the  $\tilde{r}^2$  and  $\tilde{r}^3$  terms can be used, respectively, to infer information about the bulk  $(C_BD_B)$  and surface  $(C_SD_S)$  ionic conductivity. In other words, from measurements of the electrodeposit size at the beginning of the growth phase, it is possible to deduce information about the bulk and interfacial ion transport in an electrolyte.

We investigated electrodeposition of Li under galvanostatic conditions at a range of current densities (Figure 1c) followed by an ex situ SEM observation of the nuclei size, morphology (Figure 1d), and distribution. A conventional carbonate electrolyte, that is, 1 M LiPF<sub>6</sub> in EC/DMC (1:1 vol %), was used in the study. At all current densities studied, the  $\eta_{\rm m}$  was observed at a relatively small areal capacity of the electrodeposited lithium (between 0.045–0.052 mAh/cm², depend-

ing on the current density. If the Li electrodeposit density is assumed to be the same as the bulk metal, an equivalent of 250-300 nm of Li metal is deposited by  $\eta_{\rm m}$ . The capacities for nucleation overpotential and overpotential minimum (Figure 1c) are higher for lower current densities. This may be due to extra capacity required owing to simultaneous formation of nascent SEI and Lithium nuclei at a lower rate of electrodeposition. A lower value of voltage at overpotential minimum than nucleation overpotential suggests that it is favorable for Li ions to electrodeposit on preexisting nuclei's rather than forming new nuclei embryos (Figure 1c).

To facilitate comprehensive post-mortem studies, multiple replicates of Li electrodeposited on polished stainless-steel substrates were collected and analyzed via SEM and XPS. The areal capacity for a given current density was kept fixed for each of the replicates. The morphology of the Li electrodeposits obtained from SEM analysis is reported in Figure 2A. The bare bright stainless-steel substrate can be seen underneath the Li nuclei. The nuclei are distinct in size for different current densities with smaller and densely distributed nuclei occurring at higher current densities. Larger conjoining bloblike-nuclei are visible at lower current densities, while smaller, distinct ones can be seen at higher current densities. At the lowest current density of 0.5 mA/cm<sup>2</sup> nuclei twice the size (2.25  $\mu$ m compared to 1.18  $\mu$ m) of those formed at the highest current density of 10 mA/cm<sup>2</sup> are observed. Also, higher nucleation overpotentials (e.g., 0.67 V at  $10~\text{mA/cm}^2$  compared to 0.19 V at 0.5 mA/cm<sup>2</sup>) and plateau overpotentials (e.g., 0.23 V at 10 mA/cm<sup>2</sup> compared to 0.09 V at 0.5 mA/ cm<sup>2</sup>) are observed at higher current densities. These observations can be rationalized as follows. A higher current density imparts a higher activation overpotential and mass transfer overpotential causing the overpotentials needed for the critical events to be higher. A higher nucleation overpotential  $\eta_{\rm n}$  ensures the competing factors in nuclei formation, that is, Gibbs bulk free energy  $(-\frac{4}{3}\pi r^3 F \eta_n/V)$  and the compensating surface free energy  $(4\pi r^2 \gamma)$  are larger. A larger compensating surface free energy is attained through an increased overpotential required for surface formation  $(\frac{2\gamma V}{Fr})$ , at the expense of inversely proportional critical size of the nuclei r. Hence, this leads to the formation of a greater number of smaller nuclei on the electrode surface at higher current densities.<sup>49</sup> A greater number of nuclei embryos ensures less capacity of lithium ions deposited per nucleus in the subsequent growth phase, hence smaller lithium nuclei are observed as compared to the low current density case. A similar argument can explain the densely distributed nuclei observed at higher current densities.

The electrolyte chemistry has been reported to play an important role in Lithium electrodeposition. Fluorinated additives, in particular, have received intensive attention because of their reported influence on the morphology of Li electrodeposits formed in charge/discharge battery cycling experiments. Formed in charge/discharge battery cycling experiments. Formed in electrolytes containing fluoroethylene carbonate (FEC) as a fluorinated additive. Previous studies showed that this additive breaks down to form LiF and vinylene carbonate (VC), which may electropolymerize at the reducing anode potentials to form an SEI enriched in fluorinated species. Formed in the role of FEC on the morphology and interfacial properties of Li electrodeposit nuclei, 1 M LiPF<sub>6</sub>-EC/DMC electrolytes containing 0 to 50 wt % of FEC were studied. The areal

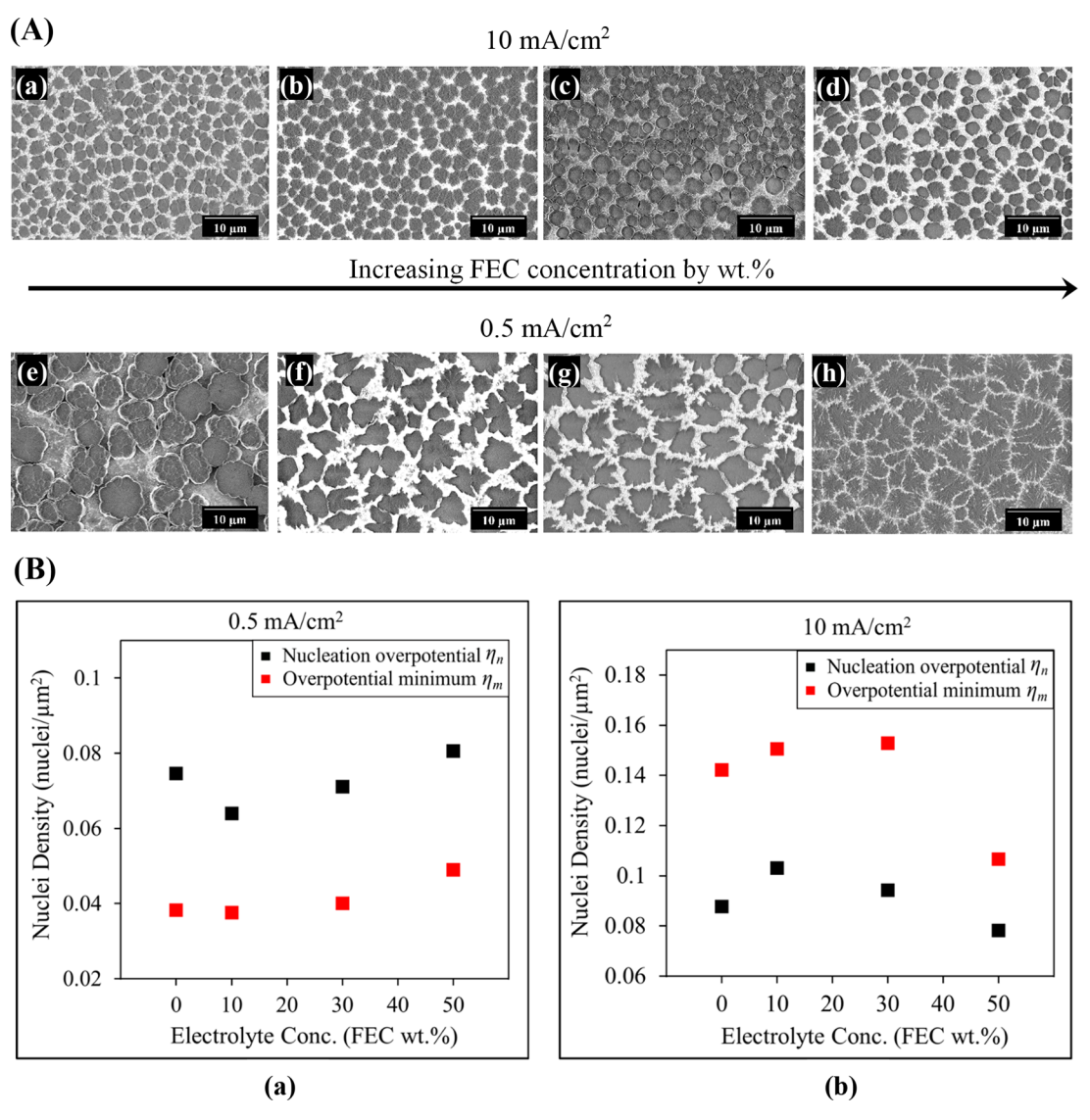


Figure 3. Effect of electrolyte chemistry on the morphology and nuclei density of lithium electrodeposits at contrasting current densities. (A) Ex situ SEM images of Li nuclei deposited on stainless-steel for current densities of 10 and 0.5 mA/cm² for increasing concentration of FEC (a,e) 0, (b,f) 10, (c,g) 30, and (d,h) 50 wt % in 1 M LiPF<sub>6</sub> EC/DMC (1:1 vol %). The total areal capacity corresponds to that of overpotential minimum (Event 2). (B) Plot of the nuclei density for varying concentration of FEC (0, 10, 30, 50 wt %) in 1 M LiPF<sub>6</sub> EC/DMC (1:1 vol %) at (a) 0.5 mA/cm² and (b) 10 mA/cm². The nucleation overpotential and overpotential minimum are shown in black and red, respectively.

capacity at overpotential minimum  $\eta_{\rm m}$  was observed to vary with electrolyte composition (i.e.,  $0.041-0.05~{\rm mAh/cm^2}$  for 10 wt % FEC,  $0.037-0.045~{\rm mAh/cm^2}$  for 30 wt % FEC, and  $0.034-0.043~{\rm mAh/cm^2}$  for 50 wt % FEC) over the range of current densities investigated (Figure S1).

The morphology of Li-electrodeposited nuclei in the FEC-enriched electrolytes are reported in Figures S2–S4 for electrolytes containing 10, 30, and 50 wt % FEC, respectively. The results show that at a fixed current density, the nuclei are enlarged and, particularly at low current density, noticeably flatter (i.e., ink stainlike, as opposed to hemispherical) at the higher FEC concentrations. The results reported in Figure 2B show that the average radius of Li electrodeposit nuclei at  $\eta_{\rm m}$  measured in the FEC-enriched electrolytes decrease with increasing current density, in essentially the same manner as observed in the baseline 1 M LiPF $_6$  EC:DMC case. The distribution of nuclei sizes was recovered from the images using the image analysis software ImageJ and represented as histograms in Figures S5–S8. For all electrolytes, the

distribution is noticeably broader at lower current densities. For example, for the baseline electrolyte (i.e., no FEC additive) at 0.5 mA/cm² the relative standard deviation of nuclei sizes is about 27%, compared to 22% at 10 mA/cm² (Figure S5). It is also apparent that in most cases the nuclei size distributions can be crudely fitted to a normal distribution, implying that the demarcations in Figure 1b are at best crude. Specifically, although a large population of nuclei appear to form at a certain time, the breadth of the distribution suggest that smaller populations of nuclei may develop at later times and grow independently during the early stages of Li deposition.

Simultaneously growing nuclei arising from instantaneous nucleation would lead to a sharper (more peaked distribution), whereas strictly continuous nucleation would lead to a flatter distribution of sizes. The situation is further complicated by the fact that a Gaussian size dispersion can also arise from coalescence/fusing of instantaneously formed nuclei and/or heterogeneous ion transport (e.g., due to a nonuniform distribution of internucleus distances produced by the finite

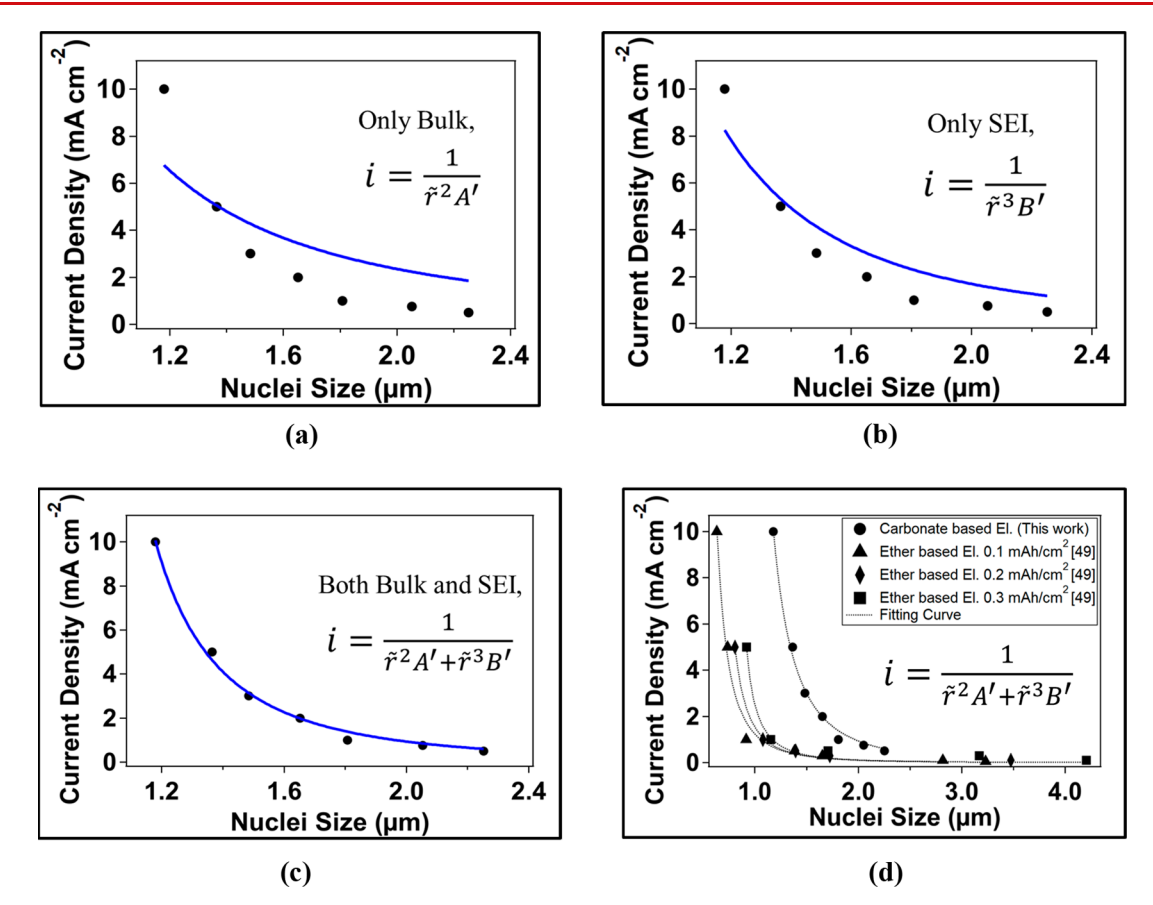


**Figure 4.** Proof of concept curve fitting at overpotential minimum and growth capacities. (a) The dependency of average nuclei radius on current density has been restricted to the effects of bulk diffusion overpotential only. (b) The dependency of average nuclei radius on current density has been restricted to the effects of SEI surface diffusion overpotential only. (c) The dependency of average nuclei radius on current density involving the synergistic effects of bulk diffusion overpotential and SEI diffusion overpotential. The electrolyte is 1 M LiPF<sub>6</sub> in EC: DMC (1:1 vol %) and the nuclei data is collected for areal capacities corresponding to Overpotential Minimum (Event 2). (d) The dependency of average nuclei radius on current density involving the synergistic effects of bulk diffusion and SEI diffusion overpotential for nuclei formed from carbonate-based electrolyte (this work) and ether-based electrolyte.

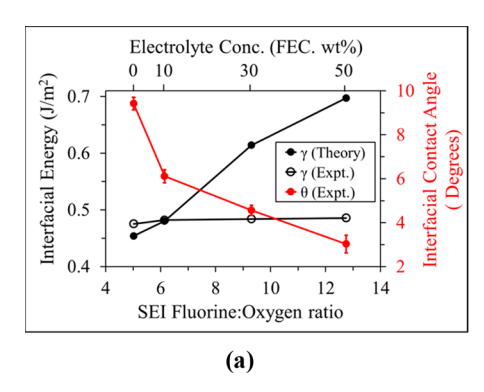
roughness of the electrode surface) to instantaneously formed nuclei. <sup>49,55-57</sup> A broader distribution at lower current densities may also indicate that internuclei diffusion coupling is important at low rates of electrodeposition. <sup>49</sup>

X-ray photoelectron spectroscopy (XPS) was performed to investigate the surface chemistry of SEI formed in electrolytes containing FEC. The results are reported in Figure 2C-E and Table S1. Although the average nuclei sizes are indifferent to the addition of FEC, distinct changes in the chemical composition of the SEI can be observed. A single dominant peak corresponding to fluorine is observed at about 685 eV; the peak increases in height as FEC content rises in the electrolytes. Analyzing the atomic % it can be inferred that a FEC-enriched electrolyte has greater concentration of fluorine groups in the SEI, that is, 71.15 at. % F for 50 wt % FEC compared to 62.41 at. % F for 0 wt % FEC (Figure 2C). Similarly by contrasting the atomic %, it can also be inferred that the fluorine to oxygen atomic % ratio (F/O) in the SEI increases significantly with addition of FEC. For 50 wt % FEC the F/O ratio is 12.75, which is approximately 250% higher than the corresponding ratio (5.02) at 0 wt % FEC.

A closer look at the high-resolution individual element spectra of Lithium and Fluorine is necessary to further understand the nature of bonding in the FEC-induced SEI. There are two peaks observed in the Li 1s spectra: LiF at 59.9

eV and Li<sub>2</sub>CO<sub>3</sub> at 57.5 eV (Figure 2. (D)). The LiF peak is enhanced for higher wt % of FEC i.e. 25.12% LiF, 74.88% Li<sub>2</sub>CO<sub>3</sub> at 50 wt % FEC compared to 10.96% LiF, 89.04% Li<sub>2</sub>CO<sub>3</sub> at 0 wt % FEC (Table S1). Similar inferences can be drawn for the F 1s spectra where two peaks are also observed: LiF at 684.9 eV and C-F at 689.1 eV (Figure 2E). Along with similar enhancement of the LiF peak, FEC-induced SEI shows a higher proportion of LiF than C-F i.e. 61.65% LiF, 38.35% C-F at 50 wt % FEC contrasted to 37.42% LiF, 62.56% C-F at 0 wt % FEC. The XPS results are consistent with earlier reports 18,50-52 and corroborate the fact that LiF-rich fluorinated SEI is formed via the decomposition of the FEC, even during the earliest stages of Li electrodeposition.

A closer look at the spatial evolution of these nuclei between the two critical events (nucleation overpotential and overpotential minimum) shall aid our understanding of the nucleation process and growth dynamics. We performed detailed galvanostatic electrodeposition studies at two contrasting current densities (0.5 and 10 mA/cm²) followed by ex situ SEM observation of the nuclei size and morphology (Figure S9). The areal capacity at the  $\eta_{\rm n}$  were recorded under these conditions: 0.009–0.016 mAh/cm² for 0 wt % FEC, 0.008–0.014 mAh/cm² for 10 wt % FEC, 0.007–0.012 mAh/cm² for 30 wt % FEC, and 0.006–0.011 mAh/cm² for 50 wt % FEC depending on 0.5 mA/cm² or 10 mA/cm.. Figure 3A



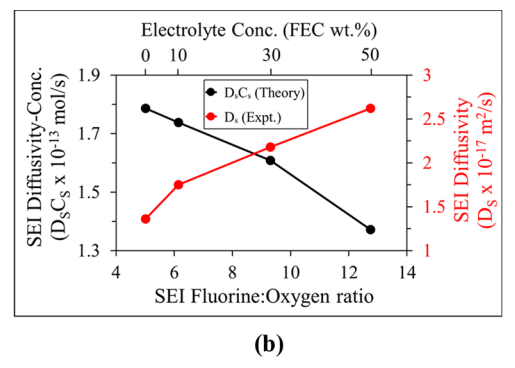


Figure 5. Effect of electrolyte chemistry/surface chemistry on the interfacial energy, interfacial contact angle, surface diffusivity, and concentration and of the SEI. (a) Plot of SEI interfacial energy (theoretically/experimentally determined) and interfacial contact angle (experimentally determined) for varying concentrations of FEC (0, 10, 30, 50 wt %) in 1 M LiPF<sub>6</sub> EC/DMC (1:1 vol %) electrolyte and corresponding fluorine to oxygen ratio in the SEI layer. (b) Plot of SEI surface diffusivity-concentration (theoretically determined) and SEI surface diffusivity (experimentally determined) for varying concentration of FEC (0, 10, 30, 50 wt %) in 1 M LiPF<sub>6</sub> EC/DMC (1:1 vol %) electrolyte and corresponding fluorine to oxygen ratio in the SEI layer.

reports the analogous areal capacities recorded at  $\eta_{\rm m}$ . The areal density of the nuclei for both events were also estimated from the SEM images and plotted in Figure 3B. Overall, densely distributed nuclei occur for the higher current density (10 mA/cm²) at both events and at all electrolyte compositions. As mentioned earlier, a high current density gives rise to a higher nucleation overpotential at the interface, which leads to formation of a greater number of nuclei. 49

At the lower current density of  $0.5 \text{ mA/cm}^2$ , the nuclei sizes observed at  $\eta_n$  are smaller than at  $\eta_m$ . For example, for 0 wt % FEC, the average nucleus size (radius) is about  $1.81 \ \mu m$  compared to  $2.25 \ \mu m$  at  $\eta_m$  (Figure S9(e) vs Figure 3A(e)). The areal coverage of the nuclei is also higher at  $\eta_m$  (e.g., for 0 wt % FEC at  $0.5 \ \text{mA/cm}^2$ , the nuclei density is about  $0.075 \ \text{nuclei/}\mu\text{m}^2$  at  $\eta_n$  compared to  $0.038 \ \text{nuclei/}\mu\text{m}^2$  at  $\eta_m$ ). This observation spans all electrolyte chemistries and suggests that as the formed nuclei grow, they also tend to agglomerate/fuse. The decreasing overpotential after the peaking and subsequent plateauing of the overpotential curve (Figure 1c, Figure S1) in between these events is consistent with growth on preexisting nuclei. Simultaneous growth and agglomeration would lead to less dense, larger nuclei at low current density.

There is a significant change in morphology of the electrodeposits at a lower current density for the FEC-enriched electrolytes as is apparent from Figure 3A(e-h) (at  $\eta_{\rm m}$ ) and Figure S9(e-h) (at  $\eta_n$ ). At 0.5 mA/cm<sup>2</sup>, the nuclei size and density increase with the incorporation of FEC. The morphology of the nuclei transition from hemispherical three-dimesional (3D) spherical structures to flat two-dimensional (2D) structures. These differences are apparent even at 10 wt % FEC but are more pronounced at higher FEC content. Figure S10 shows the effect the fluorinated electrolyte chemistry at an even lower current density of 0.05 mA/cm<sup>2</sup>. The planarizing effect is evident at even lower FEC contents and the nuclei appear to flow into each other, more fully utilizing the surface area of the stainless-steel substrate. The capacity at the critical events are also lower (see Figure S11a), implying that the 2D nuclei require lower capacity to nucleate and grow at low current densities. None of these electrolyte chemistry-dependent effects are observed at a high current density of 10 mA/cm<sup>2</sup> (see Figure 3A(a-d)) indicating that their origins are associated with changes in deposition dynamics induced by the FEC. Previously, XPS analysis revealed that the SEI formed on Li in a FEC-containing electrolyte is enriched in fluorine-containing species, including LiF. Also, a LiF-rich SEI has been postulated to have high surface energy and to pose lower barriers to surface diffusion. S8-61 Higher interphase mobility enhances rearrangement of Li ions prior to deposition, facilitating more uniform and compact electrodeposition. Hence, it is relevant to investigate the role of physical parameters such as interfacial energy and surface diffusion in the planarizing effect of fluorinated additives.

The theory correlating the current density with the observed nuclei size (eq 2) serves as a useful tool for unravelling the contributions made by surface energetic, bulk, and surface transport parameters. The squared/cubic relationship of the nuclei radius with the applied current density i.e.  $i = \frac{1}{r^2A' + r^3B'}$ contains coefficients (A' and B') which have surface diffusivity  $(D_S)$ , surface concentration  $(C_S)$ , and interfacial energy  $(\gamma)$ embedded in them. A proof of concept analysis was performed to fit the current density with the observed nuclei size  $\tilde{r}$  at  $\eta_{\rm m}$ using eq 2 (see SI on curve fitting). Three distinct cases were considered to determine the relevance of each mass transfer overpotential in the growth phase as demonstrated in Figure 4a-c. In Case 1 (Figure 4a), we ignore surface diffusion (i.e.,  $A' \gg B'$ ) and in Case 2 (Figure 4b) we ignore the contribution to the transport overpotential originating from ion migration in the electrolyte bulk (i.e.,  $B' \gg A'$ ). In Case 3 (Figure 4c) we consider the case where the surface and bulk diffusion make comparable contributions to the transport overpotential. The vastly improved quality of the fit for Case 3, relative to Cases 1 and 2 confirm that a combination of mass transfer overpotentials due to bulk diffusion and SEI diffusion are important in determining  $\eta_{\rm m}$ . A similar proof of concept analysis was carried out for all of the fluorinated/nonfluorinated carbonatebased electrolyte compositions studied as shown in Figure S12. Motivated by the ability of eq 2 to quantitatively replicate the iversus  $\tilde{r}$  data for the full set of carbonate electrolytes used in the study, we also compared the model predictions to literature results for ether-based electrolyte compositions studied in the work of Pei et al.<sup>49</sup> The results reported in Figure 4d show that the model predictions are in quantitative accord with the observations reported by Pei et al.; 49 the corresponding parameters are provided in Table S2. We therefore conclude that in every situation, the Case 3 physics provide the best

description of available  $\tilde{r}$  versus i data for Li electrodeposition in liquid electrolytes.

We estimated the interfacial energy  $(\gamma)$  for lithium in carbonate electrolytes with different FEC contents using contact angle measurements performed in an argon-filled glovebox. The results reported in Figure 5a and Table S3 show that  $\gamma$  increases gradually from 475 to 486 mJ/m<sup>2</sup> as the FEC content is increased from 0 to 50 wt %. Electrolyte wetting of studies (Figure S13) indeed reveal better Li wettability at higher concentration of FEC. The average contact angle formed between the electrolyte and Li ranges from 9.42° to 3.03° when the FEC content ranges from 0 wt % FEC to 50 wt % (Figure 5a). The lowering of the contact angle is consistent with the higher  $\gamma$ . Using the best-fit values of A' and B'obtained by fitting the empirical  $\tilde{r}$  versus i data using eq 2, we calculate the actual  $\gamma$ -values under conditions of the electrodeposition experiments. The results (Figure 5a) show that while the values of  $\gamma$  are comparable to the ones estimated from the contact angle experiment, those obtained by fitting the Li nucleate size data are a stronger function of FEC content ( $\gamma$  ranges from 454 to 697 mJ/m<sup>2</sup> with the addition of FEC). The mismatch between the experimentally estimated and theoretical values of  $\gamma$  can be 2-fold. First, Young's equation employed to calculate the interfacial energy is valid for interfaces with lower interfacial energy than the solid substrate (in this case lithium).<sup>62</sup> Second, the interphases formed on Li by reduction of FEC under the deposition conditions are more enriched in fluorinated species than those formed on Li in contact with the electrolyte under ambient conditions.

Electrochemical impedance spectroscopy was performed on lithium electrodeposited on polished stainless steel to determine the surface and bulk transport characteristics (Figure S15 and Figure 5b). The product of surface diffusivity and surface concentration decreases with the incorporation of FEC as shown in Figure 5b. However, the surface diffusivity of Li ions is observed to increase with increasing concentration of FEC (e.g.,  $D_S$  is  $2.62 \times 10^{-17}$  m<sup>2</sup>/s at 50 wt % FEC contrasted to  $1.36 \times 10^{-17}$  m<sup>2</sup>/s at 0 wt % FEC), a roughly 2-fold increase in  $D_s$ . A decreasing  $C_sD_s$  value therefore means that the surface concentration of Li ions at the electrode decreases quite rapidly as FEC concentration rises (Table S4). The surface concentration  $C_S$  is  $1.313 \times 10^4 \text{ mol/m}^2$  at 0 wt % FEC compared to  $0.523 \times 10^4 \text{ mol/m}^2$  at 50 wt % FEC, that is, more than a 2-fold decrease in the concentration, which is consistent with the two-step (surface ion transport → Li-ion reduction) reaction assumed in eq 2 when the surface ion transport is rate limiting.

A higher surface diffusivity indicates relatively easier 2D migration of Li ions in the fluorinated SEI, promoting more spread-out/delocalized electrodeposition. Assuming fast reduction kinetics of Li-ions at the electrode, a higher  $D_{\rm S}$  would also lower the concentration of Li ions in the SEI. This also explains the lowering of the SEI and charge transfer resistance evident in Figure S15c and is consistent with previous reports. Synergistically, high surface diffusivity and high interfacial energy of the fluorinated SEI facilitates planar electrodeposits as observed earlier for fluorinated electrolytes (10–50 wt % FEC). On the other hand, the carbonated electrolyte (0 wt % FEC) lacking such interfacial advantages forms 3D, bloblike nuclei which have higher probability of succumbing to the morphological instability that drives growth of mossy/dendritic Li electrodeposit morphologies. Recent

modeling studies have shown the SEI diffusivity<sup>63-66</sup> to be anywhere in between 10<sup>-16</sup> to 10<sup>-26</sup> m<sup>2</sup>/s and SEI surface energy<sup>12,67-69</sup> to be in between 0.18 to 0.84 J/m<sup>2</sup> with higher values  $(10^{-16} \text{ m}^2/\text{s} \text{ and } 0.84 \text{ J/m}^2)$  reported for a purely LiF interface. The range of surface diffusivity and interfacial energy values deduced by fitting eq 2 to the empirical  $\tilde{r}$  are in rough agreement with these values. Figure S15d shows further that the bulk diffusivity  $(10^{-10} \text{ m}^2/\text{s})$  of Li ions is about 7 orders of magnitude higher than the surface diffusivity  $(10^{-17} \text{ m}^2/\text{s})$ , implying that even a highly fluorinated interphase has a throttling effect on transport of Li-ions arriving from the bulk. This mismatch in bulk and interphase diffusivities will produce a rapid piling-up of ions at the electrolyte/electrode interface, ultimately leading to nonplanar mossy/dendritic electrodeposition of Li even in fluorinated electrolytes. Similarly, accumulation of Li ion vacancies underneath the SEI during Li anode stripping has been shown to be detrimental for the adherence/passivity of the SEI layer. 70 Electrolyte and interphases that lower the bulk/surface diffusivity ratio are therefore predicted to be essential for achieving compact, planar electrodeposition of Li in liquid electrolytes.

In summary, we study the effect of electrolyte chemistry on the morphology, size, density, spatial distribution, surface chemistry of early stage Li nuclei formed at different rates of electrodeposition. The underlying physics of Lithium (reactive metal) nucleation and growth through electrodeposition is elucidated. A comprehensive understanding of the galvanostatic overpotential curve and the square-cubic inverse dependency of nuclei radius on current density is demonstrated and experimentally correlated. Such a dependency reveals both bulk ion diffusion and surface ion diffusion to play an equally important role in lithium electroplating. Theoretical formulations along with aptly designed experiments also reveal interfacial dynamics of the SEI. Designing interfaces with high surface energy and high surface diffusivity is a feasible solution to eliminate dendritic morphology of electrodeposited lithium. Additional studies dealing with understanding the nucleation and growth dynamics of reactive metals are cardinal to understand the morphological and chemical instabilities originating at early stages of electrodeposition. Understanding and elimination of the instabilities at the initiation step would enable uniform and compact plating of reactive metals.

## ASSOCIATED CONTENT

## S Supporting Information

The Supporting Information is available free of charge on the ACS Publications website at DOI: 10.1021/acs.nanolett.9b03548.

Details of curve fitting, voltage response plots, nuclei distributions, SEM, XPS, impedance spectroscopy, and goniometer characterizations, coin cell fabrication, electrochemical testing methods, image analysis, and additional figures (PDF)

## AUTHOR INFORMATION

### **Corresponding Author**

\*E-mail: laa25@cornell.edu.

ORCID

Lynden A. Archer: 0000-0001-9032-2772

Notes

The authors declare no competing financial interest.

## ACKNOWLEDGMENTS

The research was supported as part of the Center for Mesoscale Transport Properties, an Energy Frontier Research Center supported by the U.S. Department of Energy (DOE), Office of Science, Basic Energy Sciences, under Award DE-SC0012673. The electron microscopy facilities made use of the Cornell Center for Materials Research Shared Facilities which are supported through the NSF MRSEC program (DMR-1719875). The interface characterization work made use of the facilities available in CESI, Cornell. The authors would like to thank John Grazul of CCMR, Cornell and Dr. Jiefu Yin of CESI, Cornell for their support in setting up the experiments.

#### REFERENCES

- (1) Zhang, J. G.; Xu, W.; Henderson, W. A. Lithium metal anodes and rechargeable lithium metal batteries; Springer International Publishing: Switzerland, 2017.
- (2) Whittingham, M. S. History, evolution, and future status of energy storage. *Proc. IEEE* **2012**, *100*, 1518–1534.
- (3) Aurbach, D.; Cohen, Y. J. Electrochem. Soc. 1996, 143, 3525-3532.
- (4) Xu, W.; Wang, J.; Ding, F.; Chen, X.; Nasybulin, E.; Zhang, Y.; Zhang, J. G. Energy Environ. Sci. 2014, 7, 513-537.
- (5) Tikekar, M. D.; Choudhury, S.; Tu, Z.; Archer, L. A. Nat. Energy 2016, 1, 16114.
- (6) Chianelli, R. R. J. Cryst. Growth 1976, 34, 239-244.
- (7) Aurbach, D.; Zinigrad, E.; Cohen, Y.; Teller, H. Solid State Ionics 2002, 148, 405–416.
- (8) Zachman, M. J.; Tu, Z.; Choudhury, S.; Archer, L. A.; Kourkoutis, L. F. *Nature* **2018**, *560*, 345.
- (9) Chandrashekar, S.; Trease, N. M.; Chang, H. J.; Du, L. S.; Grey, C. P.; Jerschow, A. *Nat. Mater.* **2012**, *11*, 311–315.
- (10) Monroe, C.; Newman, J. J. Electrochem. Soc. **2005**, 152, A396–A404
- (11) Tang, M.; Albertus, P.; Newman, J. J. Electrochem. Soc. 2009, 156, A390-A399.
- (12) Yamaki, J. I.; et al. J. Power Sources 1998, 74, 219-227.
- (13) Wood, K. N.; Kazyak, E.; Chadwick, A. F.; Chen, K. H.; Zhang, J. G.; Thornton, K.; Dasgupta, N. P. ACS Cent. Sci. 2016, 2, 790–801.
- (14) Wang, X.; Zeng, W.; Hong, L.; Xu, W.; Yang, H.; Wang, F.; Duan, H.; Tang, M.; Jiang, H. Nat. Energy 2018, 3, 227.
- (15) Li, G.; Archer, L. A.; Koch, D. L. Phys. Rev. Lett. 2019, 122, 124501
- (16) Miao, R.; Yang, J.; Feng, X.; Jia, H.; Wang, J.; Nuli, Y. J. Power Sources 2014, 271, 291–297.
- (17) Qian, J.; Henderson, W. A.; Xu, W.; Bhattacharya, P.; Engelhard, M.; Borodin, O.; Zhang, J.-G. *Nat. Commun.* **2015**, *6*, 6362.
- (18) Suo, L.; Xue, W.; Gobet, M.; Greenbaum, S. G.; Wang, C.; Chen, Y.; Yang, W.; Li, Y.; Li, J. *Proc. Natl. Acad. Sci. U. S. A.* **2018**, *115*, 1156–1161.
- (19) Gordin, M. L.; Dai, F.; Chen, S.; Xu, T.; Song, J.; Tang, D.; Azimi, N.; Zhang, Z.; Wang, D. ACS Appl. Mater. Interfaces 2014, 6, 8006–8010.
- (20) Aurbach, D.; Pollak, E.; Elazari, R.; Salitra, G.; Kelley, C. S.; Affinito, J. J. Electrochem. Soc. 2009, 156, A694-A702.
- (21) Kim, H.; Wu, F.; Lee, J. T.; Nitta, N.; Lin, H.-T.; Oschatz, M.; Cho, W. I.; Kaskel, S.; Borodin, O.; Yushin, G. Adv. Energy Mater. 2015, 5, 1401792.
- (22) Choudhury, S.; Archer, L. A. Adv. Electron. Mater. 2016, 2, 1500246.
- (23) Cheng, X.-B.; Zhang, R.; Zhao, C.-Z.; Wei, F.; Zhang, J.-G.; Zhang, Q. Adv. Sci. 2016, 3, 1500213.
- (24) Lin, D.; Liu, Y.; Cui, Y. Nat. Nanotechnol. 2017, 12, 194-206.
- (25) Zheng, G.; Lee, S. W.; Liang, Z.; Lee, H.-W.; Yan, K.; Yao, H.; Wang, H.; Li, W.; Chu, S.; Cui, Y. Nat. Nanotechnol. **2014**, *9*, 618–623.

(26) Zhang, J.; Yang, X.; Wang, R.; Dong, W.; Lu, W.; Wu, X.; Wang, X.; Li, H.; Chen, L. J. Phys. Chem. C 2014, 118, 20756–20762.

- (27) Zhang, Y.; Wang, W.; Tang, H.; Bai, W.; Ge, X.; Wang, X.; Gu, C.; Tu, J. J. Power Sources 2015, 277, 304–311.
- (28) Lee, H.; Lee, D. J.; Kim, Y.-J.; Park, J.-K.; Kim, H.-T. J. Power Sources 2015, 284, 103-108.
- (29) Haregewoin, A. M.; Wotango, A. S.; Hwang, B.-J. *Energy Environ. Sci.* **2016**, *9*, 1955–1988.
- (30) Umeda, G. A.; Menke, E.; Richard, M.; Stamm, K. L.; Wudl, F.; Dunn, B. *J. Mater. Chem.* **2011**, *21*, 1593–1599.
- (31) Wang, X.; Hou, Y.; Zhu, Y.; Wu, Y.; Holze, R. Sci. Rep. 2013, 3, 1401.
- (32) Bates, J. B.; Dudney, N. J.; Gruzalski, G. R.; Zuhr, R. A.; Choudhury, A.; Luck, C. F.; Robertson, J. D.; et al. *Solid State Ionics* **1992**, 53-56, 647–654.
- (33) Li, J.; Ma, C.; Chi, M.; Liang, C.; Dudney, N. J. Adv. Energy Mater. 2015, 5 (4), 1401408.
- (34) Kanno, R.; Murayama, M. J. Electrochem. Soc. 2001, 148, A742-A746.
- (35) Lu, Y.; Tikekar, M.; Mohanty, R.; Hendrickson, K.; Ma, L.; Archer, L. A. Adv. Energy Mater. 2015, 5, 1402073.
- (36) Song, J.; Lee, H.; Choo, M.-J.; Park, J.-K.; Kim, H.-T. Sci. Rep. **2015**, *5*, 14458.
- (37) Cheng, X. B.; Hou, T. Z.; Zhang, R.; Peng, H. J.; Zhao, C. Z.; Huang, J. Q.; Zhang, Q. Adv. Mater. 2016, 28, 2888–2895.
- (38) Stone, G. M.; Mullin, S. A.; Teran, A. A.; Hallinan, D. T.; Minor, A. M.; Hexemer, A.; Balsara, N. P. J. Electrochem. Soc. 2012, 159, A222-A227.
- (39) Giles, J. R. M.; Gray, F. M.; Maccallum, J. R.; Vincent, C. A. *Polymer* 1987, 28, 1977–1981.
- (40) Khurana, R.; Schaefer, J. L.; Archer, L. A.; Coates, G. W. J. Am. Chem. Soc. **2014**, 136, 7395–7402.
- (41) Pan, Q.; Smith, D. M.; Qi, H.; Wang, S.; Li, C. Y. Adv. Mater. 2015, 27, 5995–6001.
- (42) Choudhury, S.; Mangal, R.; Agrawal, A.; Archer, L. A. Nat. Commun. 2015, 6, 10101.
- (43) Gurevitch, I.; Buonsanti, R.; Teran, A. A.; Gludovatz, B.; Ritchie, R. O.; Cabana, J.; Balsara, N. P. *J. Electrochem. Soc.* **2013**, *160*, A1611—A1617.
- (44) Yang, C. P.; Yin, Y. X.; Zhang, S. F.; Li, N. W.; Guo, Y. G. Nat. Commun. 2015, 6, 8058.
- (45) Zhamu, A.; Chen, G.; Liu, C.; Neff, D.; Fang, Q.; Yu, Z.; Xiong, W.; Wang, Y.; Wang, X.; Jang, B. Z. Energy Environ. Sci. **2012**, 5, 5701–5707.
- (46) Ji, X.; Liu, D. Y.; Prendiville, D. G.; Zhang, Y.; Liu, X.; Stucky, G. D. *Nano Today* **2012**, *7*, 10–20.
- (47) Zheng, J.; Tang, T.; Zhao, Q.; Liu, X.; Deng, Y.; Archer, L. A. ACS Energy Lett. 2019, 4 (6), 1349-1355.
- (48) Barton, J. L.; Bockris, J. O. M Proc. R. Soc. London, Ser. A 1962, 268, 485–505.
- (49) Pei, A.; Zheng, G.; Shi, F.; Li, Y.; Cui, Y. Nano Lett. 2017, 17, 1132–1139.
- (50) Zhang, X. Q.; Cheng, X. B.; Chen, X.; Yan, C.; Zhang, Q. Adv. Funct. Mater. 2017, 27, 1605989.
- (51) Markevich, E.; Salitra, G.; Chesneau, F.; Schmidt, M.; Aurbach, D. ACS Energy Lett. 2017, 2, 1321–1326.
- (52) Zhang, X. Q.; Chen, X.; Cheng, X. B.; Li, B. Q.; Shen, X.; Yan, C.; Huang, J. Q.; Zhang, Q. Angew. Chem., Int. Ed. 2018, 57, 5301–5305
- (53) Winand, R. J. Appl. Electrochem. 1991, 21, 377-385.
- (54) Vetter, K. J. Electrochemical Kinetics Theoretical Aspects; Elsevier Science: Burlington, 2013.
- (55) Fransaer, J. L.; Penner, R. M. J. Phys. Chem. B 1999, 103, 7643-7653
- (56) Penner, R. M. J. Phys. Chem. B 2002, 106, 3339-3353.
- (57) Serruya, A.; Mostany, J.; Scharifker, B. R. J. Chem. Soc., Faraday Trans. 1993, 89, 255-261.
- (58) Lu, Y.; Tu, Z.; Archer, L. A. Nat. Mater. 2014, 13, 961.

ı

(59) Gunceler, D.; Letchworth-Weaver, K.; Sundararaman, R.; Schwarz, K. A.; Arias, T. A. *Modell. Simul. Mater. Sci. Eng.* **2013**, 21, No. 074005.

- (60) Michan, A. L.; Parimalam, B. S.; Leskes, M.; Kerber, R. N.; Yoon, T.; Grey, C. P.; Lucht, B. L. *Chem. Mater.* **2016**, 28, 8149–8159.
- (61) Sun, H. H.; Dolocan, A.; Weeks, J. A.; Rodriguez, R.; Heller, A.; Mullins, C. B. J. Mater. Chem. A 2019, 7, 17782–17789.
- (62) Zhu, D.; Liao, X.; Dai, P. Chin. Sci. Bull. 2012, 57, 4517-4524.
- (63) Benitez, L.; Seminario, J. M. J. Electrochem. Soc. 2017, 164, E3159-E3170.
- (64) Guan, P.; Liu, L.; Lin, X. J. Electrochem. Soc. 2015, 162, A1798-A1808.
- (65) Yildirim, H.; Kinaci, A.; Chan, M. K.; Greeley, J. P. ACS Appl. Mater. Interfaces 2015, 7, 18985—18996.
- (66) Tasaki, K.; Goldberg, A.; Lian, J. J.; Walker, M.; Timmons, A.; Harris, S. J. *J. Electrochem. Soc.* **2009**, *156*, A1019—A1027.
- (67) Liu, Z.; Qi, Y.; Lin, Y. X.; Chen, L.; Lu, P.; Chen, L. Q. J. Electrochem. Soc. 2016, 163, A592–A598.
- (68) Jand, S. P.; Kaghazchi, P. J. Phys.: Condens. Matter 2014, 26, 262001.
- (69) Kokko, K.; Salo, P. T.; Laihia, R.; Mansikka, K. Surf. Sci. 1996, 348, 168-174.
- (70) Shi, F.; Pei, A.; Boyle, D. T.; Xie, J.; Yu, X.; Zhang, X.; Cui, Y. Proc. Natl. Acad. Sci. U. S. A. 2018, 115, 8529—8534.